OXFORD

ORIGINAL ARTICLE

# Transient Subgranular Hyperconnectivity to L2/3 and Enhanced Pairwise Correlations During the Critical Period in the Mouse Auditory Cortex

Xiangying Meng[1], Krystyna Solarana[1], Zac Bowen[1], Ji Liu[1],
Daniel A. Nagode[1], Aminah Sheikh[1], Daniel E. Winkowski[1],
Joseph P. Y. Kao[2] and Patrick O. Kanold[1,]

[1]Department of Biology, University of Maryland, College Park, MD 20742, USA, and [2]Center for Biomedical Engineering and Technology, and Department of Physiology, University of Maryland School of Medicine, Baltimore, MD 21201, USA

Address correspondence to Patrick O. Kanold, Department of Biology, University of Maryland, 1116 Biosciences Res. Bldg., College Park, MD 20742, USA. Email: pkanold@umd.edu

## Abstract

During the critical period, neuronal connections are shaped by sensory experience. While the basis for this temporarily heightened plasticity remains unclear, shared connections introducing activity correlations likely play a key role. Thus, we investigated the changing intracortical connectivity in primary auditory cortex (A1) over development. In adult, layer 2/3 (L2/3) neurons receive ascending inputs from layer 4 (L4) and also receive few inputs from subgranular layer 5/6 (L5/6). We measured the spatial pattern of intracortical excitatory and inhibitory connections to L2/3 neurons in slices of mouse A1 across development using laser-scanning photostimulation. Before P11, L2/3 cells receive most excitatory input from within L2/3. Excitatory inputs from L2/3 and L4 increase after P5 and peak during P9–16. L5/6 inputs increase after P5 and provide most input during P12–16, the peak of the critical period. Inhibitory inputs followed a similar pattern. Functional circuit diversity in L2/3 emerges after P16. In vivo two-photon imaging shows low pairwise signal correlations in neighboring neurons before P11, which peak at P15–16 and decline after. Our results suggest that the critical period is characterized by high pairwise activity correlations and that transient hyperconnectivity of specific circuits, in particular those originating in L5/6, might play a key role.

**Key words:** Auditory cortex, cerebral cortex, circuits, correlation, critical period, development, intracortical, layer 2/3, layer 5/6, mouse, refinement, subgranular, transient

## Introduction

Primary sensory cortices contain large-scale maps of sensory stimulus properties, and neurons within these areas are linked via intra- and interlaminar connections. Sensory maps and intracortical connections emerge during development, and sensory experience during a critical period in development can influence this process (Hensch 2004; Feldman 2009; Schreiner and Polley 2014). The circuit basis for this temporary sensitivity to sensory manipulations remains unclear. Shared connections can introduce activity correlations (De La Rocha

et al. 2007), which can be read out by correlation-based learning rules (Feldman 2009). Since such learning rules are crucial in development (Feldman 2009), shared connections might play an important role during the critical period. However, the topology of the functional mesoscale intra- and interlaminar circuits across development is unknown. In the primary auditory cortex (A1) of altricial species such as rodents, there is a marked increase in dendritic complexity and spine number during the postnatal period, followed by a period of spine maturation approximately after P16 in rats (McMullen et al. 1988; Schachtele et al. 2011). This period roughly corresponds to the functionally identified critical period (Zhang et al. 2001; Barkat et al. 2011). While these morphological measures show that there is a period of increased functional connectivity, the circuit topology and identity of presynaptic neurons are unknown.

Primary cortical areas perform hierarchical processing. Layer 4 (L4) receiving thalamic input whereas L2/3 (L2/3) integrates ascending input from L4 and subgranular sources as well as from diverse intralaminar and cross-hemispheric intracortical inputs (Schreiner and Winer, 2007; Atencio et al. 2009; Atencio and Schreiner 2010; Oviedo et al. 2010; Chen et al. 2011; Hackett et al. 2011; Guo et al. 2012; Meng et al. 2015; Meng et al. 2017b). A1 L2/3 neurons form a heterogeneous group of cells showing distinct spatial topologies of their associated functional circuits possibly underlying the local heterogeneity in frequency integration observed in L2/3 (Bandyopadhyay et al. 2010; Rothschild et al. 2010; Winkowski and Kanold 2013; Kanold et al. 2014; Maor et al. 2016; Meng et al. 2017b; Liu et al. 2019; Tischbirek et al. 2019). Subsets of L2/3 cells receive subgranular inputs from L5/6 (Meng et al. 2017b), and these inputs are thought to control response gain (Olsen et al. 2012; Bortone et al. 2014; Guo et al. 2017).

To investigate the nature of the changing functional circuits and the emergence of laminar processing in A1, we characterized the development of the functional L2/3 microcircuits and the functional organization of A1 in vitro using laser-scanning photostimulation (LSPS). We found transient hyperconnectivity from L4 and L5/6 during the critical period, which provided the dominant number of inputs to L2/3 at P12–16. After P20 excitatory connections refined, this refinement was paralleled by the emergence of increased diversity of L2/3 connectivity.

To investigate how functional circuit changes relate to the population responses of A1, we performed in vivo two-photon $Ca^{2+}$-imaging in anesthetized mice from before ear opening (P9–11) to adulthood (>P28). Tonal stimuli evoked cortical responses at all ages studied. During the early critical period (P15–16), neighboring A1 neurons showed the highest degree of pairwise activity correlations indicating a response sparsification after the critical period.

Together, our results indicate that distinct circuit topologies exist during the critical period in rodents. In particular, (1) inputs from L4 and subgranular L5/6 are present, which can control local activity correlations and (2) specific L2/3 subcircuits emerge in the second postnatal week resulting in response sparsification. These findings suggest that subgranular circuits might play a role in controlling activity and plasticity during the critical period.

## Materials and Methods
### Animals

All animal procedures were approved by the University of Maryland Animal Care and Use Committee. Male and female mice were raised in 12-h light/12-h dark conditions.

## In vitro LSPS

LSPS experiments were performed as previously described (Meng et al. 2015; Meng et al. 2017b; Viswanathan et al. 2017).

### Slice Preparation

Mice (C57/Bl6, Jackson Labs; P5–31) were deeply anesthetized with isoflurane (halocarbon). A block of brain containing A1 and the medial geniculate nucleus was removed, and thalamocortical slices (500 μm thick) were cut on a vibrating microtome (Leica) in ice-cold artificial cerebral spinal fluid (ACSF) containing (in mM): 130 NaCl, 3 KCl, 1.25 $KH_2PO_4$, 20 $NaHCO_3$, 10 glucose, 1.3 $MgSO_4$, 2.5 $CaCl_2$ (pH 7.35–7.4, in 95%$O_2$–5%$CO_2$). For A1 slices, the cutting angle was approximately 15° from the horizontal plane (lateral raised) and A1 was identified as described previously (Cruikshank et al. 2002; Zhao et al. 2009; Meng et al. 2015). Slices were incubated for 1 h in ACSF at 30 °C and then kept at room temperature. Slices were held in a chamber on a fixed-stage microscope (Olympus BX51) for recording and superfused (2–4 mL/min) with high-Mg ACSF recording solution at room temperature to reduce spontaneous activity in the slice. The recording solution contained (in mM) 124 NaCl, 5 KCl, 1.23 $NaH_2PO_4$, 26 $NaHCO_3$, 10 glucose, 4 $MgCl_2$, and 4 $CaCl_2$. The location of the recording site in A1 was identified by landmarks (Cruikshank et al. 2002; Zhao et al. 2009; Viswanathan et al. 2012; Meng et al. 2014; Meng et al. 2015; Meng et al. 2017b).

### Electrophysiology

Whole-cell recordings were performed with a patch clamp amplifier (Multiclamp 700B, Axon Instruments) using pipettes with input resistance of 4–9 M$\Omega$. Data acquisition was performed with National Instruments AD boards and custom software (Ephus) (Suter et al. 2010), which was written in MATLAB (Mathworks) and adapted to our setup. Voltages were corrected for an estimated junction potential of 10 mV. Electrodes were filled with (in mM) 115 cesium methanesulfonate ($CsCH_3SO_3$), 5 NaF, 10 EGTA, 10 HEPES, 15 CsCl, 3.5 MgATP, and 3 QX-314 (pH 7.25, 300 mOsm). Cesium and QX314 block most intrinsic active conductances and thus make the cells electrotonically compact. Biocytin or neurobiotin (0.5%) was added to the electrode solution as needed. Series resistances were typically 20–25 M$\Omega$. Photostimulation: 0.5–1 mM of caged glutamate (N-(6-nitro-7-coumarinylmethyl)-L-glutamate) (Muralidharan et al. 2016) is added to the ACSF. This compound has no effect on neuronal activity without UV light (Muralidharan et al. 2016). UV laser light (500 mW, 355 nm, 1 ms pulses, 100-kHz repetition rate, Diode-pumped solid-state laser (DPSS) Lasers, Santa Clara, CA) was split by a 33% beam splitter (CVI Melles Griot), attenuated by a Pockels cell (Conoptics), gated with a laser shutter (NM Laser), and coupled into a microscope via scan mirrors (Cambridge Technology) and a dichroic mirror. The laser beam in LSPS enters the slice axially through the objective (Olympus 10×, 0.3NA/water) and has a diameter of less than 20 μm. Laser power at the sample is less than 25 mW. We typically stimulated up to $30 \times 25$ sites spaced 40 μm apart, enabling us to probe areas of 1 mm²; such dense sampling reduces the influence of potential spontaneous events. Repeated stimulation yielded essentially identical maps. Stimuli were applied at 0.5–1 Hz. Analysis was performed essentially as described previously with custom software written in MATLAB (Meng et al. 2014; Meng et al. 2015; Meng et al. 2017a; Meng et al. 2017b). Activation profiles of neurons were produced by recording in cell-attached mode

while mapping the same region and recording action potentials (Supplementary Fig. S1). To detect monosynaptically evoked postsynaptic currents (PSCs), we detected PSCs with onsets in an approximately 50-ms window after the stimulation (Fig. 1*b*). This window was chosen based on the observed spiking latency under our recording conditions (Meng et al. 2015; Meng et al. 2017b; Viswanathan et al. 2017). Our recordings are performed at room temperature and in high-$Mg^{2+}$ solution to reduce the probability of polysynaptic inputs. We measured both peak amplitude and transferred charge; transferred charge was measured by integrating the PSC. While the transferred charge might include contributions from multiple events, our prior studies showed a strong correlation between these measures (Viswanathan et al. 2012; Meng et al. 2014; Meng et al. 2015). Traces containing a short-latency (<8 ms) "direct" response were discarded from the analysis (black patches in color-coded maps) as were traces that contained longer latency inward currents of long duration (>50 ms). The short-latency currents could sometimes be seen in locations surrounding (<100 μm) areas that gave a "direct" response. Occasionally, some of the "direct" responses contained evoked synaptic responses that we did not separate out, which leads to an underestimation of local short-range connections. Cells that did not show any large (>100 pA) direct responses were excluded from the analysis as these could be astrocytes. It is likely that the observed PSCs at each stimulus location represent the activity of multiple presynaptic cells. Layer boundaries were determined from the infrared pictures.

## Morphology

Biocytin-filled cells were processed and reported previously (Zhao et al. 2009; Deng et al. 2017; Sheikh et al. 2019). Recorded cells filled with biocytin were stained and reconstructed through Neurolucida (Version 2019; MBF Bioscience). Morphological data been used here were extracted from the built-in Sholl analysis in Neurolucida.

## In Vivo Imaging

In vivo experiments were performed in male and female *Thy1*-GCaMP6s transgenic mice (GP4.3; JAX strain 02475) (Dana et al. 2014), bred in-house. In vivo imaging was performed during postnatal days (P) 9–59, which encompasses a period of time before ear opening (P9–11; $n = 4$), ear opening, and hearing onset (P12–14; $n = 7$), the critical period for rapid auditory spectral tuning, which we split into an early (P15–16; $n = 4$) and a late window (P18–20; $n = 9$), and through to the mature adult (P28–59; $n = 9$). While studies with chronic imaging windows are possible in adult rodents (Meng et al. 2017b; Francis et al. 2018; Liu et al. 2019), these surgeries and recovery are not feasible in young animals whose skulls and brains are rapidly increasing in size. Therefore, we performed acute craniotomies and imaged the same day in anesthetized animals.

## Surgery

Mice were initially anesthetized with 4% inhaled isoflurane (Fluriso, VetOne) using a calibrated vaporizer (Matrix VIP 3000), which was reduced to 2–2.5% for the craniotomy procedure to maintain stable anesthesia. Body temperature was maintained near 37 °C with a heating block, and depth of anesthesia was monitored by toe pinch reflex and by observing the respiratory pattern of the animal. Tissue overlying the left auditory cortex

was exposed, and the skull was affixed to a custom titanium headplate using cyanoacrylate glue (Loctite Prism 454). A small circular craniotomy (3–4 mm diameter) was performed to expose the surface of the auditory cortex, as determined by skull and vascular landmarks (Stiebler et al. 1997; Dorr et al. 2007). A circular glass coverslip (5 mm, #0 thickness, Warner Instruments) was fixed to the surface of the craniotomy with 1.5–2% warm agarose (Sigma-Aldrich) to dampen pulsations and was secured with glue on the outer edges to the headplate. For mice less than P12–13 in which the ear canal was still naturally closed, a small surgical incision was made to open the ear and allow sound to enter without additional impedance.

## Wide-Field Imaging

Cortical images of wide-field GCaMP6s fluorescence in blue light were acquired at a depth of 500 μm from the surface using StreamPix software (NorPix) with either a CoolSNAP HQ2 or a CoolSNAP MYO CCD Camera (Photometrics), and with either a tandem-lens combination setup (Ratzlaff and Grinvald 1991) or a 2× objective (Nikon). Sound stimuli consisted of 1000-ms duration, sinusoidal-amplitude-modulated (SAM) tones at frequencies of 4, 8, 16, 32, and 64 kHz. Each frequency was randomly repeated five times at three sound levels: 40-, 60-, and 80-dB sound pressure level (SPL) for a total of 75 iterations.

## Two-Photon Imaging

Imaging was largely performed as described previously (Winkowski and Kanold 2013) using a two-photon microscope (Ultima, Prairie Technologies) and a MaiTai DeepSee laser (SpectraPhysics), equipped with a GaAsP photodetector module (Hamamatsu) and resonant scanners. Excitation at 900 nm was focused at 150–200 μm beneath the pia for supragranular layers 2/3 and 300–380 μm for thalamorecipient L4 imaging (see Table 1); thus, the lower part of L4 was not imaged. Regions within A1 (∼300 × 300 μm) were scanned at 30 Hz through a 20×, 0.95 NA water-immersion objective (Olympus), with image resolution at 0.58 μm/pixel. Body temperature was maintained at 37 °C using a homeothermic blanket system (Harvard Apparatus) and a flexible probe to monitor internal temperature. For mice younger than P20, the flexible probe was secured externally to the ventral surface of the animal. Isoflurane was maintained at 1–1.5% for the duration of the imaging session. To prevent cortical cooling and to avoid network cortical dysregulation, a constant perfusion of warmed saline (35–37 °C, Warner Instruments Inline heater) was allowed to flow over the coverslipped surface of the craniotomy (Kalmbach and Waters 2012).

## Auditory Stimulation

Sound stimuli were generated using custom software in MATLAB, presented and attenuated using Tucker-Davis Technologies RX6 processor, ED1 electrostatic speaker driver, and PA5 programmable attenuator, and delivered through an ES1-free field speaker placed close to the contralateral (right) ear. Sound intensity was calibrated with a microphone (Brüel & Kjær 4944-A). Sounds were played at 60-dB SPL (about 30 dB above mouse hearing threshold). Auditory stimuli consist of 400-ms-long SAM tones (5-Hz modulation, cosine phase), ranging from 4 to 64 kHz at quarter octave spacing (thus spanning four octaves). Each of these 17 stimuli was repeated 10 times with a 6-s
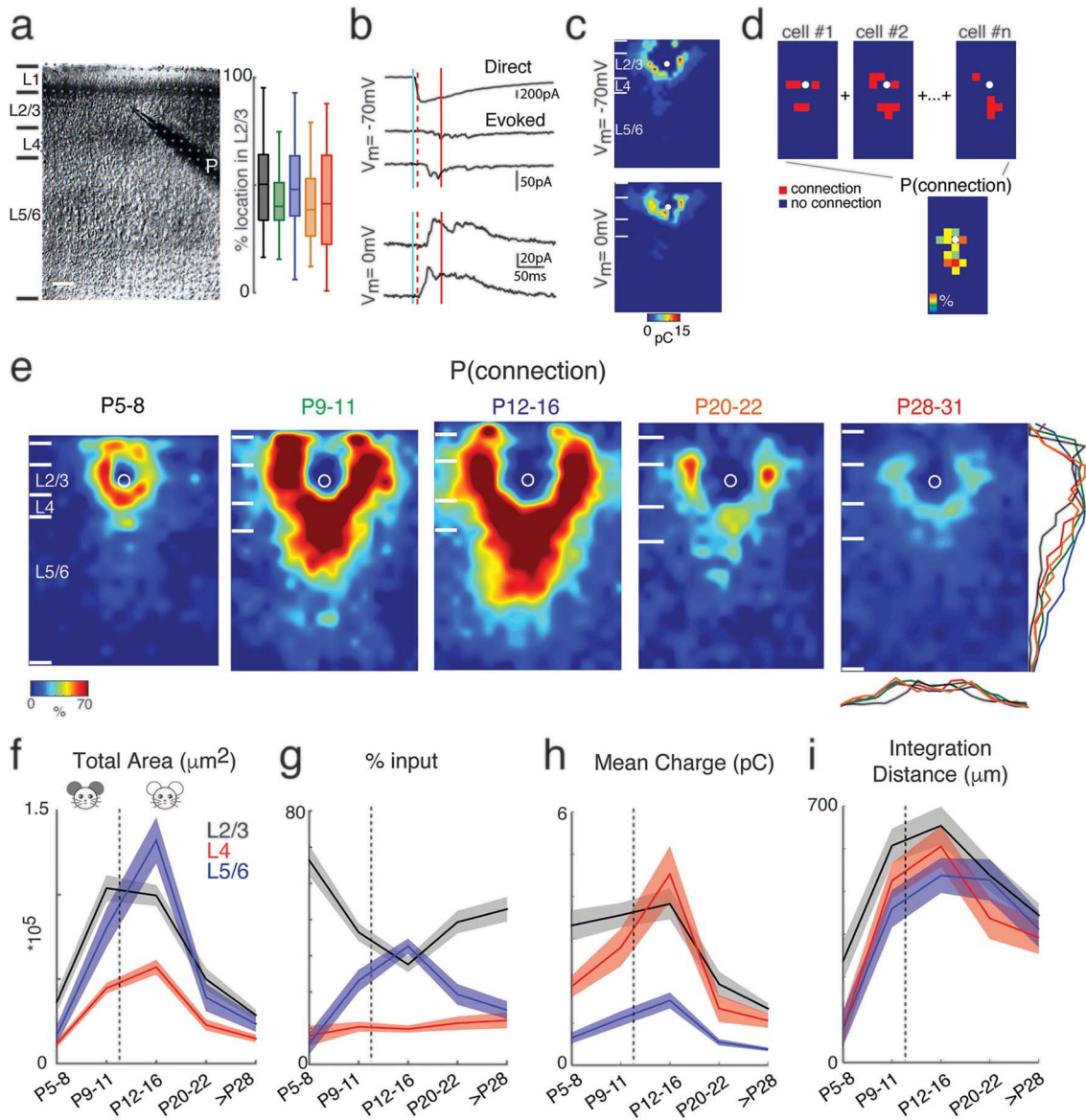
**Figure 1.** Excitatory circuits to L2/3 neurons rearrange during development. (*a*) Left: Infrared image of a brain slice with patch pipette on an L2/3 neuron. Stimulation grid is indicated by the blue dots. The black bars on the left of the image are the layer boundaries (Pia, boundary between L1 and L2/3, boundary between L2/3 and L4, boundary between L4 and L5/6, and the boundary between L6 and white matter). The scale bar represents 100 μm. Right: Relative position of recorded cells within L2/3 for different age groups (P5–8: black; P9–11: green; P12–16: blue; P20–22: orange; P28–31: red). 0% represents the border with L4 and 100% represents the border with L1. There is no significant difference between different groups (Multicomparison, P5–8 vs. P9–11: $P = 0.41$; P5–8 vs. P12–16: $P = 0.92$; P5–8 vs. P20–22: $P = 0.16$; P5–8 vs. P28: $P = 0.37$; P9–11 vs. P12–16: $P = 0.83$; P9–11 vs. P20–22: $P = 1$; P9–11 vs. P28: $P = 1$; P12–16 vs. P20–22: $P = 0.54$; P12–16 vs. P28–31: $P = 0.86$; P20–22 vs. P28–31: $P = 0.95$). (*b*) Whole-cell voltage clamp recordings with holding potentials at −70 (top) and 0 mV (bottom) to investigate excitatory and inhibitory synaptic connections, respectively. Shown are example traces evoked by photostimulation at different locations. The solid blue line indicates the time of photostimulation. The dashed red line marks 8-ms poststimulus, which is the minimal latency for synaptic responses. The solid red line marks the end of the 50-ms event analysis window. (*c*) Pseudocolor maps show EPSC (left) and IPSC (right) charge at each stimulus location. White circle indicates the soma location. Horizontal bars indicate layer borders; bar length represents 100 μm. (*d*) Cartoon illustrating the calculation of the average spatial probability (P [connection]) maps. Input maps are aligned to soma and for each relative location, the average number of cells in which a response could be evoked from this location is calculated. (*e*) Average maps of spatial connection probability (aligned to soma, white circle) of excitatory connections in different age groups. The pseudocolor indicates the connection probability. White horizontal bars indicate averaged laminar borders and are 100 μm long. Traces at the bottom of the average map of P28–31 indicate the columnar marginal distributions. The colors of the traces match the colors of the titles of the average maps in different age groups. Traces below and at the right side of the average map of P28–31 indicate the laminar marginal distributions of the connection probability maps and illustrate the temporary increase of inputs from L5/6. (*f*) The mean (solid) and SEM (shadow) of total area of inputs from L2/3 (black), L4 (red) and L5/6 (blue) to L2/3 neurons in different age groups. The excitation areas for P9–11 and P12–16 groups originating from L2/3, L4, and L5/6 show significant increase comparing among four age groups (P values are in Supplementary Table 1). (*g*) The mean (solid) and SEM (shadow) of relative area of excitatory inputs from L2/3 (black), L4 (red), and L5/6 (blue) to L2/3 neurons in different age groups. The relative area from L5/6 reaches its peak at P12–16 (P values are in Supplementary Table 3). (*h*) The mean (solid) and SEM (shadow) of the average EPSC charge of inputs from L2/3 (black), L4 (red), and L5/6 (blue) to L2/3 neurons in different age groups. After P28, the connection strength becomes weaker compared to other age groups (P values are in Supplementary Table 2). (*i*) The mean (solid) and SEM (shadow) of the distance of 80% of excitatory inputs to each L2/3 cell originating from L2/3 (black), L4 (red), and L5/6 (blue). The integration distances of L2/3, L4, and L5/6 inputs begin to increase at early age up to P16 and decreases at P28–31 (P values are in Supplementary Table 4). The dashed lines in *f*-*i* mark the time of ear opening.

**Table 1** Animals, fields, and cell numbers imaged in vivo

| Layer | Age | Animals | Fields | Mean depth | # Cells |
|-------|-----|---------|--------|------------|---------|
| L2/3 | P9–11 | 4 | 12 | $186 \pm 7.4$ μm | 508 |
| | P12–14 | 7 | 12 | $188 \pm 6.4$ μm | 699 |
| | P15–16 | 4 | 10 | $189 \pm 4.8$ μm | 1301 |
| | P18–20 | 9 | 22 | $190 \pm 3.4$ μm | 2210 |
| | P28–59 | 8 | 15 | $189 \pm 4.1$ μm | 989 |
| L4 | P9–11 | 3 | 6 | $348 \pm 29.3$ μm | 217 |
| | P12–14 | 6 | 7 | $345 \pm 18.8$ μm | 497 |
| | P15–16 | 4 | 13 | $347 \pm 7.7$ μm | 1039 |
| | P18–20 | 8 | 21 | $348 \pm 14.6$ μm | 1264 |
| | P28–59 | 9 | 14 | $370 \pm 10.9$ μm | 846 |

interstimulus interval, for a total of 170 iterations. For each stimulus iteration, a sequence of 100 images were acquired for a duration of 3.3 s with sound onset at 1.5 s (or at about the 45th frame). To generate frequency response areas (FRAs), sounds were played either at four different dB levels (30-, 45-, 60-, and 75-dB SPL) or at six different dB levels (30-, 40-, 50-, 60-, 70-, and 80-dB SPL) with each stimulus repeated five times. For FRAs, we were limited to five trials especially in the young animals because we kept intertrial intervals long to prevent adaptation and synaptic fatigue, which can be prominent in developing brains.

## Wide-field Data Analysis

Image sequences were analyzed using custom routines in MAT-LAB (Mathworks). Images were parsed into trial-based epochs in which each frame sequence represented a single trial consisting of the presentation of a single-sound-frequency-intensity combination. For each trial, the response amplitude ($\Delta F/F$) as a function of time for each pixel was determined using the following formula, $(F–F_0)/F_0$, where $F$ corresponds to the time-varying fluorescence at a given pixel. $F_0$ was estimated by finding the 10th percentile of these fluorescence values for a given trial and pixel. For construction of activation maps, the amplitude of the $\Delta F/F$ pixel response during 1 s (i.e., ∼ four frames) after stimulus onset was averaged across time and repetitions, yielding an average response magnitude that was assigned to each pixel. To determine total responsive area for each animal, the average activation map for each sound frequency-intensity combination was binarized according to a threshold (mean + 2 standard deviation [SD] of baseline activity). Binarized activation maps were then summed across sounds and total area determined using the *regionprops* function in MATLAB and converted to real measurements (mm²) based on the spatial calibration of the optical system. The values of total area were grouped according to age and compared. To estimate baseline activity, the variability (SD) of $\Delta F/F$ values of baseline (prestimulus) frames across all stimulus presentation trials was determined for each pixel, and then averaged. This yielded a single value of baseline $\Delta F/F$ variability for each animal. The values of baseline variability were grouped either according to age or rearing condition and compared.

## Two-photon Data Analysis

Image sequences were first loaded into ImageJ (NIH) to visually examine if fluorescence responses were present and if

there was any x-y jitter present in the image sequence. Motion correction was performed using the ImageJ TurboReg plug-in. Image sequences with an abnormally large amount of motion unable to be corrected were discarded and not analyzed. Raw fluorescence signals ($F$) of auditory neurons were directly used to calculate time course traces. Cells were manually selected as ring-like regions of interest (ROIs) that cover soma but exclude cell nuclei. Pixel intensity within each ROI was averaged to generate fluorescence over time. Neuropil correction was performed by selecting a circular region with a radius of 20 μm around the cell, excluding all pixels that are contained within other ROIs. For each neuropil mask, the brightest 20% of pixels were also excluded as they might be neural processes from adjacent cells that are also tonally tuned, which otherwise will bias cell response to a smaller value or introduce irregularities in response patterns (Peron et al. 2015). The average fluorescence of this area (background fluorescence, $F_B$) was then subtracted from the cell's fluorescence at each time point. Changes in fluorescence ($\Delta F/F$) were calculated with the following equation (Kerlin et al. 2010; Chen et al. 2012): $[(F − r^*F_B)—(F_0 − r^*F_B)]/(F_0 − r^*F_B)$, where $F_0$ is estimated by taking the fifth-percentile value of the entire subtracted fluorescence trace (for some cells 10th-percentile value is chosen to avoid negative $F_0$), and $r$ is the contamination ratio 0.7 (Peron et al. 2015). A responsive cell was defined as a cell that responds to at least one of the presented stimuli significantly (ANOVA between baseline and stimulus activity, $P < 0.001$). Remaining analysis was performed only on responding cells. Mean time course traces were generated by averaging fluorescence traces over ten repeats. Frequency-tuning curves were determined by taking the maximum ($\Delta F/F$) from the mean time course trace across the frames following sound onset. Best frequency (BF) was then defined as the peak of the frequency-tuning curve (the tone that elicits the maximum $\Delta F/F$ at 60 dB).

Noise correlations (NC) (trial-to-trial response variability) were calculated by taking the individual response to each repeat of a sound stimulus, subtracting out the mean response to that particular stimulus and measuring the covariance of the concatenated responses from every single trial of different stimuli. When trial number is small for each stimulus, signal correlations (SC) can be strongly biased by NC (Rothschild et al. 2010; Rothschild et al. 2013). To overcome this bias, we also calculated corrected SC based on Rothschild et al. (Rothschild et al. 2010):

$$SC_{corrected}(i, j) \triangleq \frac{cov_{corrected}(r_i, r_j)}{\sqrt{cov(r_i, r_i) \cdot cov(r_j, r_j)}}$$

Unlike Rothschild et al. 2010, we used the uncorrected expression for $\text{cov}(r_i, r_i)$ in the denominator because in practice, $\text{cov}_{\text{corrected}}(r_i, r_i)$ can yield negative values for particular $r_i$.

## Cell-attached Recordings and Ca$^{2+}$ Imaging of Action Potentials in Vitro

Cell-attached patch clamp recordings were performed in vitro in voltage clamp to simultaneously measure spiking activity and $\Delta F/F$ (Goncalves et al. 2013). Thalamocortical slices containing A1 were prepared as described above. The extracellular recording solution consisted of ACSF containing (in mM) 130 NaCl, 3 KCl, 1.25 KH$_2$PO$_4$, 20 NaHCO$_3$, 10 glucose, 1.3 MgSO$_4$, and 2.5 CaCl$_2$ (pH 7.35–7.4, in 95% O$_2$–5% CO$_2$). Action potentials were recorded extracellularly in loose-seal cell-attached configuration (seal resistance typically 20–30 M$\Omega$) in voltage clamp mode. Borosilicate glass patch pipettes were filled with normal ACSF diluted 10% and had a tip resistance of approximately 3–5 M$\Omega$ in the bath. Data were acquired with a Multiclamp 700B patch clamp amplifier (Molecular Devices), low-pass filtered, and digitized at 10 kHz using Ephus (Suter et al. 2010). In order to preserve physiological ion concentrations in the imaged cells, we did not patch imaged neurons but evoked action potentials with a bipolar stimulus electrode placed in L1 or L2/3 to stimulate the apical dendrites of pyramidal cells (pulse duration of 1–5 ms). Data were analyzed offline using MATLAB.

## Statistics

Results are plotted as means $\pm$ SD unless otherwise indicated. Populations were compared with a ranksum or Student's $t$-test (based on Lilliefors test for normality) and deemed significant if $P < 0.05$.

## Results

### Mapping of Inter- and Intralaminar Circuits to L2/3 via LSPS Shows Transient Hyperconnectivity of Excitatory Circuits at P12–16

To investigate the maturation of inter- and intralaminar connections to L2/3 neurons in A1, we applied LSPS with caged glutamate (Shepherd et al. 2003; Meng et al. 2014; Meng et al. 2015; Meng et al. 2017b) to map the spatial connectivity of excitatory and inhibitory inputs to L2/3 neurons in A1 of C57/BL6 mice aged P5–31. This age range encompasses a period of time before ear opening (P9–11), the critical period for auditory spectral tuning, and through to the mature adult (>P28) (Willott and Shnerson 1978; Geal-Dor et al. 1993; Zhang et al. 2001; Barkat et al. 2011). LSPS induces action potentials in targeted neurons when the laser beam is close to the soma or proximal dendrites, where a high concentration of glutamate receptors (GluRs) is present. We performed cell-attached recordings from cells across the cortical layers at these ages to identify the locations in which photostimulation evokes APs in each cell ($N = 189$ neurons). These recordings showed that most photostimulation-evoked APs of L5/6, L4, and L2/3 cells (latencies $\leq 50$ ms) were evoked close to the soma at all ages (Supplementary Fig. S1). This is consistent with our prior cell-attached recordings at these ages (Viswanathan et al. 2012; Meng et al. 2015; Meng et al. 2017b) and indicates that the spatial resolution of our LSPS technique does not vary across age.

To visualize the spatial pattern of excitatory inputs of each cell, we performed whole-cell patch recordings and targeted the laser pulse to multiple distinct stimulus locations. The neurons under the stimulation sites were activated by the laser pulse and generated action potentials. If targeted neurons were connected to the patched cells, we were able to record PSCs. Cells were held at a membrane potential of $-70$ mV ($\sim E_{Cl}$) to isolate EPSCs or at 0 mV ($\sim E_{glut}$) to isolate IPSCs (Meng et al. 2015; Meng et al. 2017b). The targeted stimulus locations spanned the entire extent of A1, thus enabling us to probe the entire two-dimensional connectivity pattern of excitatory and inhibitory inputs to a given cell over 1 mm$^2$ (Fig. 1a). Since sublaminar circuit differences exist in L2/3 of A1 (Meng et al. 2017b), we ensured that the relative laminar locations of sampled cells in each age group were similar (Fig. 1a). Activation of GluRs on the cell body and the proximal dendrites caused large-amplitude short-latency direct events (Fig. 1b). Since synaptic currents have a distinct latency (>8 ms), we separated direct and synaptic events using a latency criterium (Fig. 1b) (Meng et al. 2015; Meng et al. 2017b). The connection strengths were quantified by calculating the postsynaptic current (PSC) charge (Meng et al. 2015; Meng et al. 2017b) and indicated as color in contour maps (Fig. 1c). Our recordings showed that L2/3 cells in A1 received excitatory input from within L2/3 as well as from L4 and L5/6 (Fig. 1c).

We performed LSPS in 155 L2/3 cells (P5–8: $n = 25$, P9–11: $n = 21$, P12–16: $n = 32$, P20–22: $n = 29$, P28–31: $n = 48$) from 46 mice (P5–8: $n = 6$ mice; P9–11: $n = 7$ mice; P12–16: $n = 7$ mice; P20–22: $n = 6$ mice; P28–31: $n = 20$ mice) and examined the connectivity pattern of excitatory inputs. To visualize connectivity pattern changes over the population of cells, individual LSPS maps were aligned to the cell body position and averaged (Meng et al. 2015; Meng et al. 2017b); the result is a spatial map of connection probability (Fig. 1d,e). From the averaged maps, we observed that L2/3 cells at all ages received inputs not only from within L2/3 but also from other cortical layers (Fig. 1e). Qualitative inspection of these maps revealed that the spatial profiles changed with development.

To quantify the laminar changes, we identified laminar borders for each cell from the DIC images and calculated the input profile from each layer (Meng et al. 2015; Meng et al. 2017b). To visualize and quantify the differences between cells, we determined for each cell the total area in each layer where stimulation evoked excitatory PSC (EPSC) in L2/3 neurons. We find that L2/3 cells received input from within L2/3 as well as from L4 from the youngest ages on. Both L2/3 and L4 inputs increased after P5–8, peaked at P9–16, and then decreased (Fig. 1f, Supplementary Fig. S2). In contrast, subgranular L5/6 inputs increased from P5–8 until P12–16 and then decreased to P20–22. Thus, there was a temporary increase of excitatory inputs to L2/3, in particular at P12–16 for subgranular L5/6 inputs. The increase in area was largest for subgranular inputs (P12–16 vs. P5–8: 795% for L5/6 vs. 481% for L4 and 272% for L2/3). These data indicate a temporary increase in the amount of intracortical synaptic connectivity and in particular from subgranular sources over development. To further quantify the balance of intra- to interlaminar inputs, we next determined the relative input the L2/3 neurons receive from each layer. This analysis confirmed that subgranular input to L2/3 neurons is highest at P12–16 (Fig. 1g, Supplementary Fig. S2). Besides the number of inputs, the effective synaptic strength contributes to the functional laminar connectivity. To test if synaptic strength from each layer also changed over development, we plotted the mean EPSC charge and total charge for EPSCs evoked from each layer (Fig. 1h, Supplementary Fig. S2). While the mean synaptic strength for intralaminar inputs

to L2/3 remained constant from P5–16, interlaminar inputs, in particular those from L4, strengthened until P16 (Fig. 1h, Supplementary Fig. S2). The total charge from all layers increased from P5. The intralaminar input to L2/3 reached its peak at P9–16, whereas the input from L4 and L5/6 reached its peak at P12–16 (Supplementary Fig. S2). Both input strength and total input decreased after this period in all layers with the largest decrease occurring in L4 (P12–16 vs. >P28: 407% for L5/6 vs. 428% for L4 and 285% for L2/3). These results indicate a temporary expansion and strengthening of interlaminar inputs to L2/3 during the critical period.

Since our thalamocortical slices contain the tonotopic axis, the distance of where presynaptic cells are located in the rostro-caudal axis is a proxy for integration along the frequency axis (Meng et al. 2017b). When quantitatively comparing the rostro-caudal spread or integration distance of inter- and intralaminar inputs at the different ages, we find that L2/3 inputs originated from a narrow region at P5–8 and that the integration distance increased thereafter, peaking at P12–16 (Fig. 1i, Supplementary Fig. S2). The integration distance in all layers decreased by P28–31 and decreases were smallest in L5/6 (P12–16 vs. >P28 129% for L5/6 vs. 150% for L4 and 144% for L2/3). Thus, our results indicate that there is a temporary period of hyperconnectivity of intracortical excitatory circuits in development, which supports integration across the tonotopic axis.

## Transient Hyperconnectivity of Inhibitory Circuits to L2/3 Cells at P12–16

Our results show a substantial remodeling of excitatory connections. We next investigated if inhibitory connections also change over development. We mapped inhibitory connections by holding cells at 0 mV (Fig. 1b). Average maps of connection probability across ages appeared different, generally showing a similar developmental trajectory to excitatory input map changes (Fig. 2a, Supplementary Fig. S3). This was confirmed quantitatively: the total area generating inhibitory input in L2/3 increased with age until P16 and then decreased (Fig. 2b, Supplementary Fig. S3, the total inhibitory area of P12–16 vs. P5–8, 579% for L5/6, 413% for L4 and 624% for L2/3). In contrast to excitatory inputs, inhibitory inputs from L4 and L5/6 did not show a relative increase during development (Fig. 2c, Supplementary Fig. S3). The fraction of input from within L2/3 increased, while L4 and L5/6 inputs showed modest decreases. The total charge originating from each layer also increased until P12–16 (Supplementary Fig. S3).

The mean inhibitory PSC (IPSC) charge from within L2/3 was largest at P12–16, while inputs from L4 were strongest between P9 and P16 (Fig. 2c, Supplementary Fig. S3). In contrast to excitatory inputs, inhibitory inputs from L5/6 showed an increase in integration distance with age, indicating a lack of tonotopic refinement (Fig. 2e, Supplementary Fig. S3). Thus, together with the changes in excitatory and inhibitory connections, these data show that there is extensive remodeling of excitatory and inhibitory connections to L2/3 neurons, but that the spatial pattern is distinct for each. Our results indicate that there is a temporary increase in relative excitatory but not inhibitory inputs from L4 and L5/6 during the critical period.

## Transient EI Imbalance to L2/3 Cells at P9–11

Given that both excitatory and inhibitory circuits change over development, and since the spatial and temporal patterns of these changes appeared different, we hypothesized that the balance of excitation and inhibition was changing over development. Studies in the visual cortex have suggested that maturation of functional inhibition, and thus the balance of excitation and inhibition (EI balance), is a prime driver of critical period plasticity (Hensch 2004). To determine the functional and spatial balance of excitation and inhibition, we calculated the EI balance of inputs from each layer based on the area as well as the charge of excitatory and inhibitory inputs (Meng et al. 2015; Meng et al. 2017b) (Fig. 2f–h). This analysis showed that the EI peak and area ratios increased and were of much larger magnitude for inputs from L5/6 than from L2/3 and L4. This indicates an overall excitatory effect of L5/6 inputs while inputs from the other layers were balanced. Moreover, there was a large transient increase in EI area for subgranular inputs due to the unmatched increase in excitatory and inhibitory inputs from these layers (the total excitatory area of P12–16 in L5/6 increased to ∼ eight times that of P5–8, whereas the total inhibitory area of P12–16 in L5/6 only increased by ∼ six times). In contrast, EI balance based on charge decreased over development due to significant increases in IPSC charge, possibly due to the change of GABA receptor subunit composition. Thus, there is a transient EI increase for subgranular inputs to L2/3 just after ear opening at the onset of the critical period. This imbalance indicates a transient increase in excitation originating from L5/6. Together with the increased EI amplitude ratio of L5/6 versus L2/3 and L4 inputs, this suggests an overall increased excitatory effect from L5/6 in the critical period.

## Emergence of Circuit Diversity by P28

Our prior studies showed that circuits to L2/3 could be diverse (Meng et al. 2017b). To quantify the emergence of this diversity, we calculated the correlation of the LSPS maps of the sampled cells. We find that correlations for both excitatory and inhibitory maps increased from P5–8 to P9–11, remained constant at P12–16, and then decreased by P28–31 (Fig. 3). These results indicate that L2/3 neurons form a relatively homogenous population based on intracortical circuit topology during the critical period and that circuit diversity emerges after P16.

## Morphological Complexity of L2/3 Neurons Increases Over Development

Our functional connection results show transient hyperconnectivity of both excitatory and inhibitory circuits during development. To investigate whether the increased connectivity is due to the morphological development of L2/3 cells, we reconstructed 37 recorded L2/3 cells across different age groups (P5–8: $n = 11$; P12–16: $n = 11$; >P28: $n = 16$) and analyzed their dendrites. This analysis indicated that L2/3 cells showed the greatest complexity in terms of number of nodes and ends at approximately P28–31 (Fig. 4), consistent with reports from rabbit A1 (McMullen et al. 1988). Moreover, Sholl analysis results (Fig. 4c) showed that most branch intersections of L2/3 cells at young age (P5–8) were within approximately 100 μm from the cell body and spread out to approximately 200 μm after P12–16. Comparing cells at P12–16 and P28–31 showed that the dendritic branch intersections in the older group tend to occur further away from the soma (range from ∼ 300 to 800 μm). Together, these results indicated that L2/3 cell morphology became more complex during development. Thus, the temporal peak in connectivity from L5/6 is not due to morphological changes in L2/3 neurons but due to functional circuit changes.
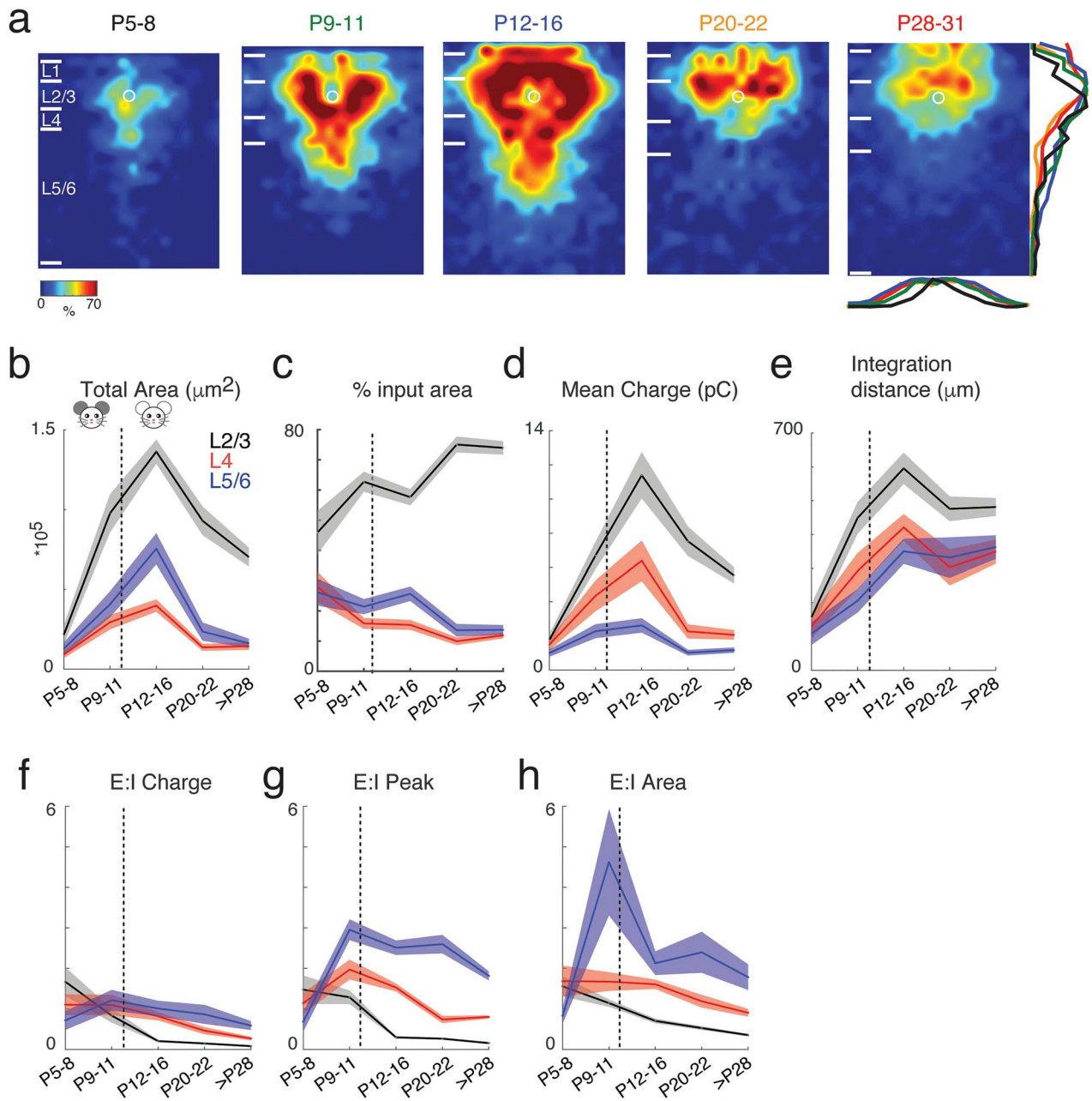
**Figure 2.** Inhibitory circuits to L2/3 neurons rearrange during development. (*a*) Average maps (aligned to soma, white circle) of inhibitory connection probability in different age groups. The pseudocolor indicates connection probability. White horizontal bars indicate averaged laminar borders and are 100 μm long. Traces at the bottom of the average map of P28–31 indicate the columnar marginal distributions. The colors of the traces match those of titles of the average maps in different age groups. Traces below and at the right side of the average map of P28–31 indicate the laminar marginal distributions of the connection probability maps. (*b*) The mean (solid) and SEM (shadow) of total area of inputs from L2/3 (black), L4 (red), and L5/6 (blue) to L2/3 neurons in different age groups. The inhibitory area for P9–11 and P12–16 groups originating from L2/3, L4, and L5/6 shows significant increases when comparing among four age groups (*P* values are in Supplementary Table 5). (*c*) The mean (solid) and SEM (shadow) of relative area of inhibitory inputs from L2/3 (black), L4 (red), and L5/6 (blue) to L2/3 neurons in different age groups. L2/3 cells receive more local inputs originating inside L2/3 during development (*P* values are in Supplementary Table 7). (*d*) The mean (solid) and SEM (shadow) of the average IPSC charge of inputs from L2/3 (black), L4 (red), and L5/6 (blue) to L2/3 neurons in different age groups. The connection strength from L2/3, L4, and L5/6 to L2/3 cells increases after P5 and reach the pick at P12–16 (*P* values are in Supplementary Table 6). (*e*) The mean (solid) and SEM (shadow) of the distance of 80% of inhibitory inputs to each L2/3 cell originating from L2/3 (black), L4 (red), and L5/6 (blue). The integration distance of L2/3, L4, and L5/6 increases during development (*P* values are in Supplementary Table 8). (*f*) The mean (solid) and SEM (shadow) of the EI charge ratio from L2/3 (black), L4 (red), and L5/6 (blue) cells. EI charge ratio decreases with age (*P* values are in Supplementary Table 9). (*g*) The mean (solid) and SEM (shadow) of the EI peak ratio from L2/3 (black), L4 (red), and L5/6 (blue) cells. EI peak has similar trends as EI charge (*P* values are in Supplementary Table 10). (*h*) The mean (solid) and SEM (shadow) of the EI area ratio from L2/3 (black), L4 (red), and L5/6 (blue) cells. EI area has similar trends as EI charge and EI peak (*P* values are in Supplementary Table 11). The dashed lines in *b*–*h* mark the time of ear opening.
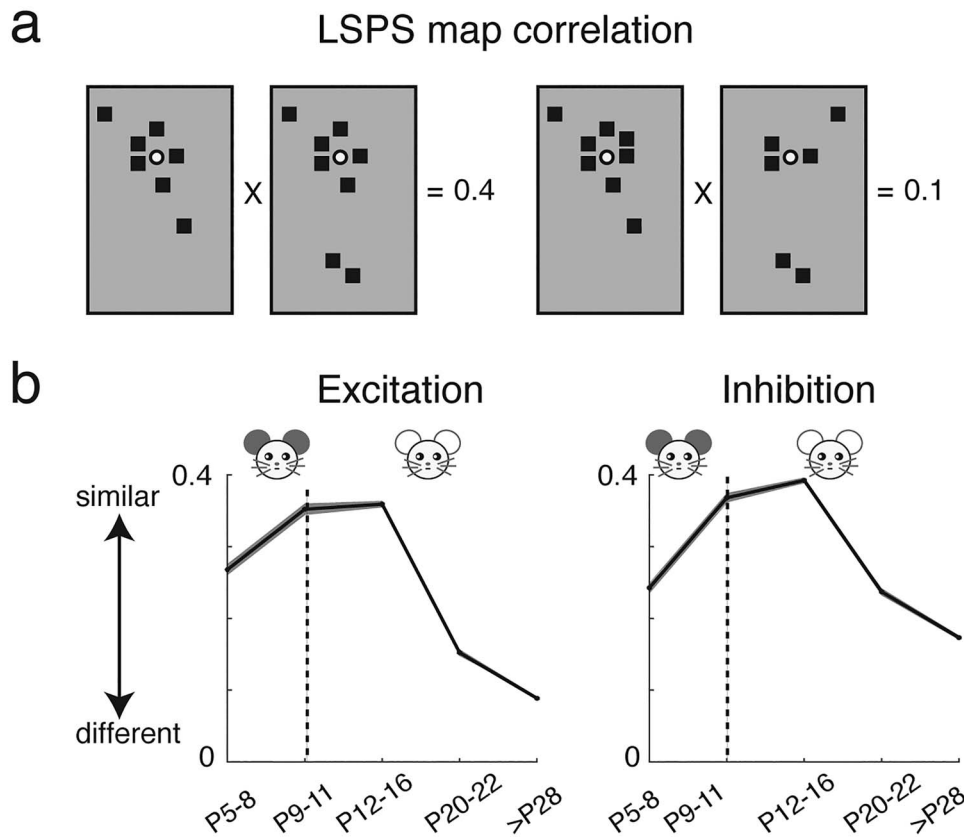
**Figure 3.** Functional circuits to L2/3 neurons show more diversity after P20. (*a*) Graphical representation of calculation of pairwise correlation between two maps. Each black square represents the area that has monosynaptic connection to the recorded cell. For the pairwise correlation calculation, we set its value to one and set the area that has no monosynaptic connections to zero. (*b*) The mean (solid) and SEM (shadow) of the pairwise correlations between all excitatory (left) and inhibitory (right) maps. The connection maps of L2/3 cells become less similar after P16 and connection maps in adult mice are more heterogeneous than those at younger ages (*P* values are in Supplementary Table 12). The dashed line in each panel marks the time of ear opening.

## Auditory Cortical Area Changes Over the Course of Hearing Development

Our in vitro results show that circuits impinging on L2/3 neurons dynamically change over development (Fig. 3). This change in circuits is likely to result in changes in the functional properties and population relationships of A1 neurons. We thus investigated the sound-evoked responses of A1 during the same developmental time frame.

We first investigated the emergence of functional auditory responses in auditory cortex. To visualize the sound-driven activity of neurons, we used wide-field and two-photon $Ca^{2+}$-imaging in *Thy1*-GCaMP6s (GP4.3; JAX strain 024275) mice (Dana et al. 2014). We performed in vivo imaging during postnatal days P9–59, which encompasses a period of time before ear opening (P9–11), the critical period for auditory spectral tuning, and through to the mature adult (P28–59; Table 1) (Willott and Shnerson 1978; Geal-Dor et al. 1993; Zhang et al. 2001; Barkat et al. 2011). To delineate more precisely the events within the critical period, we further subdivided this age group into an early (P15–16) and late (P18–20) critical period. In early development (<P12), the closed ear canals and fluid-filled middle ear can attenuate sounds. Thus, to provide a more comparable sound transmission to the tympanic membrane and to explore if A1 cells could respond to sounds at this young age, we surgically opened the ear canals in the youngest age group.

To localize auditory cortex and to delineate developmental changes in its macroscale organization, we performed wide-field imaging ($\sim 3 \times 3$ mm) of global GCaMP6s signal with tone presentation of various frequencies and sound levels (Fig. 5a) (P9–11 $n = 7$ mice, P12–14 $n = 5$ mice, P15–16 $n = 4$ mice, P18–20 $n = 8$ mice, >P28 $n = 7$ mice). We defined the auditory cortex as the cortical area showing sound-evoked changes in fluorescence. Auditory evoked responses were present as early as P9. The auditory responsive area increased after P11 and peaked in the critical period (P18–20) (P9–11 vs. P18–20; P < 0.01; multicomparison), consistent with prior microelectrode studies (Zhang et al. 2001) (Fig. 5b,c). The levels of spontaneous activity were largest before ear opening (P9–11) (Fig. 5c), likely driven by peripherally generated spontaneous activity (Siegel et al. 2012; Wang and Bergles 2015). A1 is defined as the central tonotopic area of the auditory cortex. After P14 rostro-caudally oriented tonotopic gradients were present allowing the identification of A1, AAF, and A2 (Meng et al. 2017b; Francis et al. 2018; Liu et al. 2019). Together, these results show that auditory responses emerge in the auditory cortex before ear opening and confirm that tonotopic maps can be detected after P14.

## A1 Neurons Respond to Sound From P9 Onwards and are Least Frequency-selective During the Critical Period

Having observed widespread sound-evoked activation in auditory cortex as early as P9, we next characterized the response
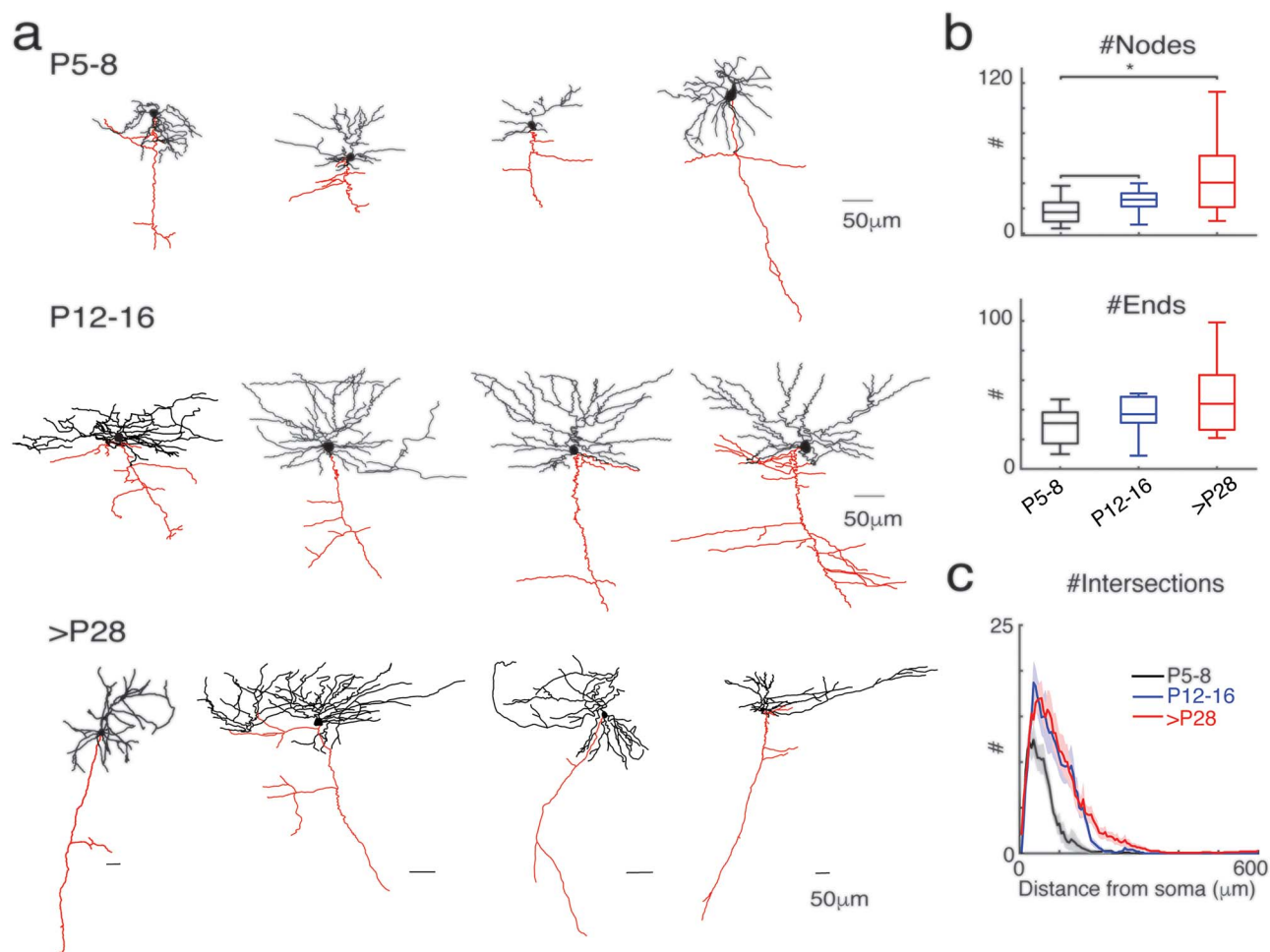
**Figure 4.** The complexity of cell morphology increases with age. (*a*) Examples of reconstructed L2/3 cells from different age groups. Dendrites are indicated in black and axons in red. (*b*) Quantification of morphological properties: the total number of nodes (upper) and ends (lower). Cells in L2/3 at P28–31 group have the most nodes and ends. (*c*) Sholl analysis. The plot shows the number of intersection of sequential serial spheres (5 μm steps) centered on the soma with the cell's dendrites as a function of radial distance. Thick line shows mean across cells and shaded area for standard error.

properties of single A1 neurons in L4 and L2/3 to tonal stimuli over development (L2/3 150–200 μm depth; L4 300–450 μm depth; Table 1) by in vivo two-photon $Ca^{2+}$ imaging ($300 \times 300$ μm; 30-Hz frame rate) (Fig. 5d,e, Supplementary Fig. S4).

We used a sound level of 60 dB across all developmental ages to identify how networks process an identical acoustic stimulus in their environment. This sound level is above threshold for the ages studied (Supplementary Fig. S5). Consistent with the wide-field results, tone presentations could evoke fluorescence increases (ΔF/F) in neurons as early as P9 (before natural ear opening) (Fig. 5d, Supplementary Fig. S5). To characterize sound-evoked responses, we varied the frequency of the presented tone and determined how many cells were driven by tonal stimuli and for each cell, determined the sound frequency that evoked the largest average response (BF) (Fig. 5e, Supplementary Fig. S5). We found that the numbers of responding cells increased until P15–16 then trended lower by P20 and remained stable until adulthood (Fig. 6a), consistent with sparse responses observed using in vivo recordings (Hromadka et al. 2008; Liang et al. 2018). Moreover, this maximum responsiveness is consistent with our LSPS experiments showing that the amount of excitatory connections to L2/3 peaks around P12–16 (Fig. 1). Thus, the

temporary peak in the number of responding cells could potentially be due to the transient peak in excitatory input to L2/3 cells.

Tuning curves (FRAs) in many auditory structures are "V-shaped," with a single-frequency selective area showing decreased frequency selectivity with increased sound level. Microelectrode studies of rodent A1 drew contradicting conclusions regarding the development of frequency selectivity: A1 cells either become more (Zhang et al. 2001; Chang and Merzenich 2003; Carrasco et al. 2013) or less (de Villers-Sidani et al. 2007) frequency-selective over development. We measured the normalized bandwidth to 60-dB stimuli using a peak-related threshold ($BW_{60\%}$) to characterize changes in tonal receptive fields over development (Figs 5e and 6b). Since many cells at P9–11 did not show clear "V-shaped" response peaks, we did not determine the bandwidth at these ages. After an initial increase, the $BW_{60\%}$ of both L4 and L2/3 neurons decreased from P15–16 into adulthood, indicating an increase in frequency selectivity (Fig. 6b). We confirmed this result using a second measure that did not require "V-shaped" receptive fields (Supplementary Fig. S5f). These results are consistent with previous microelectrode (Zhang et al. 2001; Chang and Merzenich 2003) and whole-cell
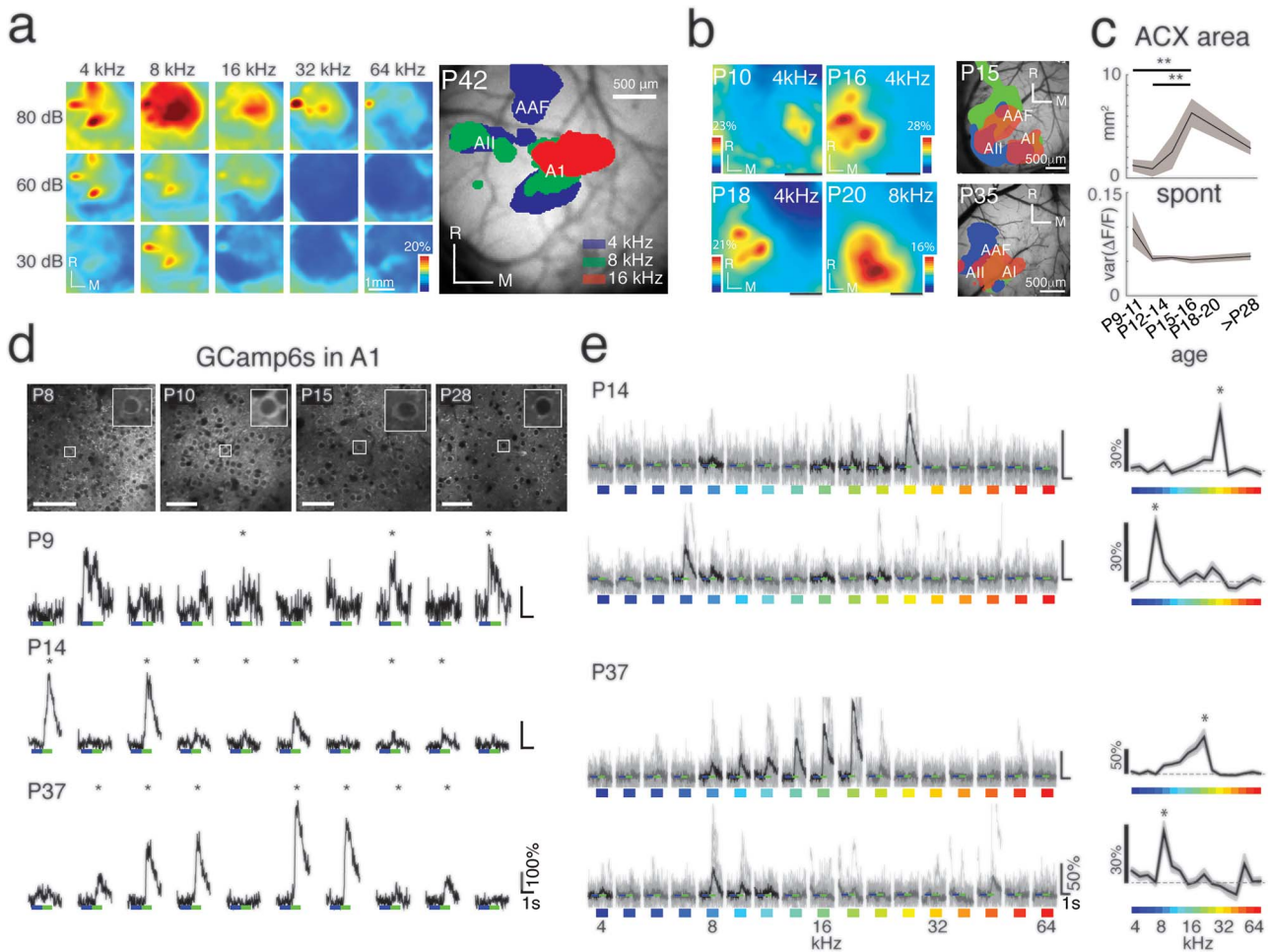
**Figure 5.** Wide-field and two-photon $Ca^{2+}$ imaging reveals early tone-evoked responses and changes in the auditory cortical area with age. (*a*) Sound-evoked wide-field fluorescence changes in a P42 *Thy1*-GCaMP6s mouse in response to tones of various frequencies and sound levels. Panel to the right shows an image of a craniotomy with typical location of blood vessels, with overlapped frequency-specific evoked responses. (*b*) Panels depict representative auditory response areas in four animals at P10, P16, P18, P20, to example tones (Scale bars = 1 mm), and exemplar tonotopic maps from two additional animals at P15 and P35 (Scale bars = 500 μm). (*c*) Top shows total auditory area (in mm²) over development. Total auditory area reaches maximum at P18–20. *P* values from multicomparison are shown in Supplementary Table 13. (*d*) Top: GCaMP6s-expressing cells at different ages. Bottom: Individual time course traces from each BF stimulus repeat for the exemplar cells at P9 (32 kHz tone), P14 (26.9 kHz tone), and P37 (19 kHz tone). Asterisks (*) indicate the responses that passed our significance criterion (*P* < 0.01). (*e*) Sample time course traces for four representative neurons from a P14 and P37 animal responding to all 17 frequencies presented (Black lines indicate mean of significant responses (*P* < 0.001), and gray lines indicate individual repetitions from each trace.) Tuning curves for each of these cells are shown on the right, with the detected BF ("*").

voltage-clamp recordings (Sun et al. 2010). Thus, our results indicate that over development, there is an initial broadening of tuning curves and increased recruitment of A1 neurons by sounds likely due to increased excitatory connections. This developmental stage is then followed by a period of receptive field refinement and a sparsification of the representation of pure tones in A1. Such fine-tuning of response selectivity and sparsification is consistent with the refinement of excitatory connections (Fig. 1).

## Correlated Activity Between Neurons Peaks at P15–16

Our in vitro results indicate a temporary strengthening and broadening of interlaminar inputs to L2/3 as well as increased circuit similarity, in particular during the critical period. These temporary changes might lead to increased pairwise activity correlations between neurons. Thus, we calculated both neuronal pairwise NC, which reflect stimulus-independent, trial-to-trial covariance, and SC, which represent stimulus-driven correlated activity (corrected for NC) (Averbeck et al. 2006; Rothschild et al. 2010; Winkowski and Kanold 2013; Liu et al. 2019).

Pairwise correlations can depend on the distance between the neurons (Levy and Reyes 2012; Ko et al. 2013; Winkowski and Kanold 2013; Liu et al. 2019). Thus to first examine age differences, we focused on nearby cell pairs and calculated the average pairwise correlations between L2/3 cells in a local area (within 50–100 μm of each cell; Fig. 6c). We found that NCs were highest in the youngest age group (P9–11) and were greater than SCs. This suggests that A1 neurons at this age receive weak feedforward (presumably thalamic) input (Barkat et al. 2011) and are most strongly driven by intracortical spontaneous activity (Siegel et al. 2012). After P12–14, SCs increased, consistent with increased shared excitatory input (Fig. 1). Moreover, increased SCs were also seen in L4 after P11 (Fig. 6d) suggesting increased shared thalamic input consistent with in vitro studies (Barkat et al. 2011). SCs in L2/3 and L4 were highest at P15–16 and SCs
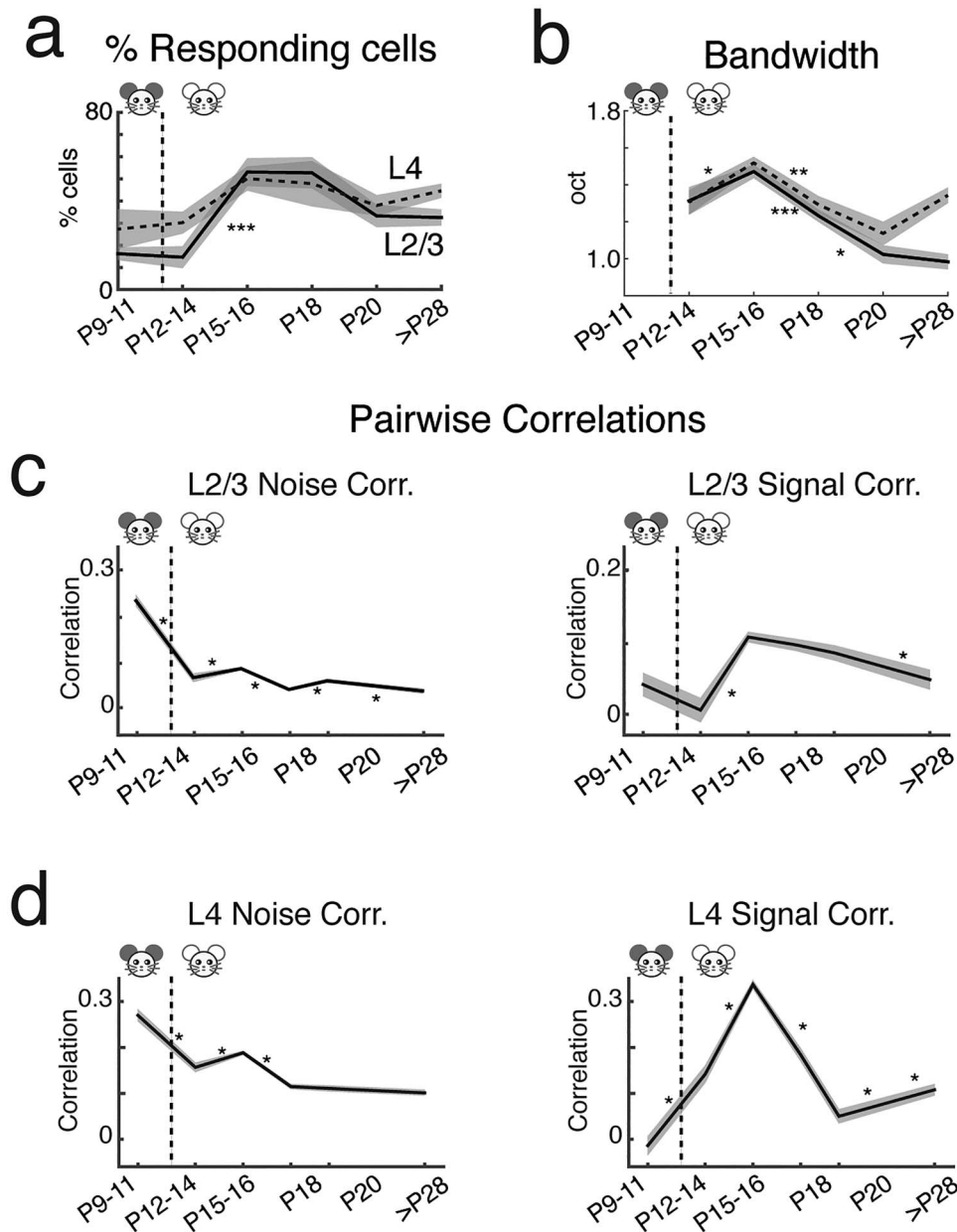
**Figure 6.** A1 single-cell response properties characterized by two-photon $Ca^{2+}$ imaging. (*a*) Fraction of responding cells was low at P9–11 and P12–14 but increases at P15–16 especially in L2/3. The fraction of responding cells decreased by P18–20 and remained stable until adulthood (adult L4 = 44.6% tone-responsive cells; adult L2/3 = 32.5% tone-responsive cells) (Supplementary Tables 14 and 15). (*b*) Bandwidth (BW) for 60% peak criterion. The BW of L2/3 cells peak temporarily at approximately P15. (*P* values are in Supplementary Tables 18 and 19, *: $P < 0.05$, **: $P < 0.005$, ***: $P < 0.0005$). (*c,d*) The mean (solid) and standard error (shadow) of NC and SC between cell pairs in L2/3 (*c*) and L4 (*d*). Correlated activity between neurons changes over development. L2/3 and L4 signal and NC within 50–100 μm are plotted over development (mean ± SEM). NCs are highest prior to ear opening (P9–11 L2/3 NC = 0.24 ± 0.006, L4 NC = 0.27 ± 0.006) and are greater than SCs in both cortical layers (L2/3 SC = 0.041 ± 0.008, L4 SC = −0.014 ± 0.010). After ear opening (P12–14), NCs decrease (L4 NC = 0.16 ± 0.005, L2/3 NC = 0.066 ± 0.005) while L4 SCs begin to increase (L4 SC = 0.142 ± 0.009). SCs in L2/3 and L4 are highest during P15–16 (L2/3 SC = 0.106 ± 0.004, L4 SC = 0.337 ± 0.005; L2/3 NC = 0.086 ± 0.002, L4 NC = 0.190 ± 0.002). SCs and NCs decline after P18 to the final mature state (adult L2/3 NC = 0.037 ± 0.003, L4 NC = 0.102 ± 0.003; Adult L2/3 SC = 0.047 ± 0.007, L4 SC = 0.108 ± 0.006) (*P* values are shown in Supplementary Tables 20 and 21, *: $P < 0.05$, **: $P < 0.005$, ***: $P < 0.0005$).

declined after P16 to the final mature state. NCs also decreased from P9 to 11 to adult with a temporary peak at P15–16. Together, these results show that pairwise activity correlations show a temporary peak at P15–16.

## Discussion

In vitro circuit analysis and in vivo multiscale imaging in mice over the first weeks of life were used to identify the development of mesoscale circuitry and functional responses in A1. Our results reveal changes in both intracortical connectivity and network activity over development. The observed transient intracortical connections with age and mesoscale changes in sound-evoked responses delineate distinct developmental periods. In particular, we identify a transient hyperconnectivity between subgranular layers (L5/6) and supragranular layers (L2/3) during the critical period, suggesting that L5/6 might play an important role during the critical
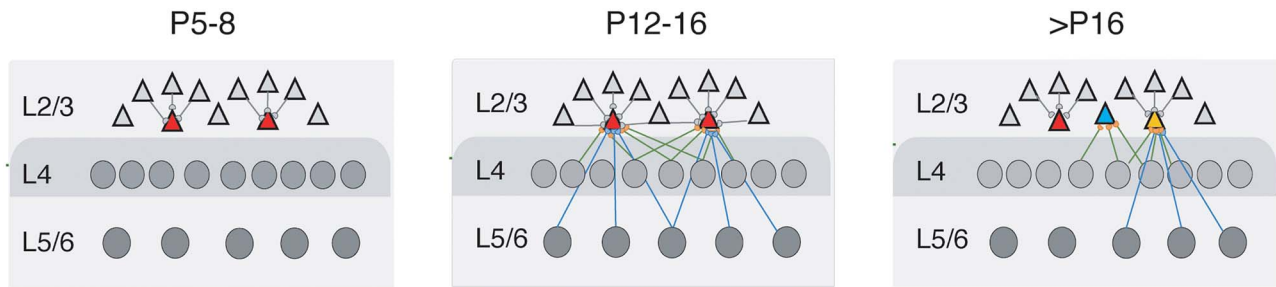
**Figure 7.** Summary of circuit changes in A1 over development. Graphic summary of L2/3 circuit development based on the functional excitatory connections. Color in L2/3 marks different cell types based on functional connections. Green: cells with local connections; orange: cells with major connections from L2/3 and L4 and few from L5/6; and grey: cells with major connections from L2/3, L4, and L5/6. We use similar colors for L4 and L5/6 cells because potential diversity is unknown. For the P5–8 group, most cells have very local connections inside L2/3. During early development (P9–11 and P12–16), most cells in L2/3 receive long-distance inputs from L4 and L5/6. Compared to P9–11, cells at P12–16 receive more inputs from L5/6. After P16, the connection pattern for L2/3 cells become more diverse.

period. The schema in Fig. 7 summarizes our circuit level results.

Here, we studied the intracortical circuits to L2/3 neurons using LSPS. The direct canonical ascending pathway of sensory information to L2/3 neurons is through L4, which increases after P9. Our results also show a temporary increase in excitatory connections from subgranular layers that can also carry sensory information. On the one hand, these layers encompass L6, which can be thalamorecipient (de Venecia and McMullen 1994; Constantinople and Bruno 2013; Crocker-Buque et al. 2015; Ji et al. 2015; Intskirveli et al. 2016; Mease et al. 2016; Slater et al. 2019; Williamson and Polley 2019) and contains upper subplate neurons, which are retained as L6b in the adult (Marx et al. 2017; Viswanathan et al. 2017; Hoerder-Suabedissen et al. 2018). On the other hand, L5/6 neurons receive long-distance connections from other sensory modalities such as vision as well as inputs from motor and frontal areas (Schroeder and Foxe 2002; Banks et al. 2011; Nelson et al. 2013; Schneider et al. 2014; Morrill and Hasenstaub 2018) (Winkowski et al. 2018), and L5/6 neurons could potentially function as a gain control circuit to regulate L4 and L2/3 responses to sensory stimuli (Olsen et al. 2012; Vélez-Fort and Margrie 2012; Bortone et al. 2014). Subgranular inputs to L2/3 show a transient maximal input between P12 and 16 and show a spatially broad distribution across the tonotopic axis suggesting broad frequency integration of this input. Thus, the temporary increase in subgranular input to L2/3 can add additional, potentially broadly tuned, thalamorecipient activity to L2/3 in parallel to the L4 to L2/3 pathways. Since deep subplate neurons are the first cortical neurons to respond to sound and to show topographic organization (Wess et al. 2017), this pathway could prime topographic responses in L2/3 and thus provide a potential parallel source of topographically thalamic input to L4. Indeed, observations from the visual cortex have suggested that plastic changes in L2/3 can precede those in L4 (Trachtenberg et al. 2000; Trachtenberg and Stryker 2001). Moreover, deep sub-plate neurons are required for normal critical period plasticity to occur (Kanold and Shatz 2006). While these results have been interpreted based on subplate inputs to L4, (Kanold 2009; Kanold and Luhmann 2010) the existence of subplate inputs across the cortical extent (Viswanathan et al. 2017) suggests that subplate and L6b neurons might affect or even coordinate cortical plasticity across layers.

We find high NCs in P9–11 mice, consistent with cortical activity driven by spontaneous peripheral and central activity patterns (Feller et al. 1996; Garaschuk et al. 2000; Adelsberger et al. 2005; Hanganu et al. 2006; Tritsch et al. 2007; Tritsch et al.

2010; Siegel et al. 2012; Wang and Bergles 2015; Babola et al. 2018). However, during this period, A1 can respond to sounds as well. Our results show that A1 can respond to sounds before ear opening in mice, consistent with electrophysiological findings in ferrets (Wess et al. 2017). These results are also consistent with sound-evoked brainstem responses in P7 rats (Geal-Dor et al. 1993). Thus, during this early period, both spontaneous cochlear activity as well as external sounds can contribute to the activity in A1.

We find that L4 SCs increase around P12, coinciding with thalamocortical strengthening (Barkat et al. 2011), and that pairwise local activity correlations are highest at P15–16 (the early critical period). Our in vitro LSPS results show that intralaminar and ascending inputs to L2/3 increase between P5 and P16, while subgranular inputs show a transient maximal input between P12 and 16, which might be a major determinant of the high pairwise correlations during the critical period. These results suggest that transient circuits from subgranular layers L5/6 might contribute to the critical period.

Typically, the critical period is characterized by altering the period of sensory deprivation (Insanally et al. 2009; Barkat et al. 2011; Caras and Sanes 2015; Mowery et al. 2015). Here, we find high pairwise correlations in L2/3 combined with peak responsiveness to auditory stimuli at P15–20, suggesting that sensory manipulation during this window could have maximal impact. Our results, therefore, identify a circuit substrate of the critical period time window as a period when neurons respond robustly to many stimuli, and when neighboring neurons have high pairwise correlations indicating that they share tuning properties. Our circuit analysis suggests that this time window is defined both by ascending excitatory and inhibitory inputs, particularly from subgranular layers. Subgranular layers are composed of multiple cell classes with diverse connectivity (Games and Winer 1988; Prieto and Winer 1999; Winer and Prieto 2001; Petrof et al. 2012; Kim et al. 2014), and L5/6 cells play a variety of roles such as the NTSR1-positive L6 neurons, which are involved in gain control (Olsen et al. 2012; Bortone et al. 2014; Guo et al. 2017). Recent results have indicated that activity manipulations during the critical period can cause gain changes in auditory cortex neurons (Chambers et al. 2016). Our work would suggest that these gain changes result from altered connectivity from L5/6 cells to their target neurons. Our results suggest that these gain control circuits are calibrated during the critical period to environmental conditions. Additionally, prior work has identified a key role for the maturation of inhibitory circuits in regulating the critical period (Hensch 2004). Results described here suggest

that subgranular circuits, which innervate both excitatory and inhibitory cortical neurons (Bortone et al. 2014), might play a role in this process. Thus, while the effect of sensory manipulation in early development is evident in thalamorecipient neurons, key regulators of this plasticity might reside in subgranular layers or the cortical subplate (Kanold and Shatz 2006).

NCs decrease over development in both layers even though intralaminar and interlaminar excitatory connectivity increased, which would be expected to result in increased NCs. As inhibitory connectivity also increases, these in vivo observations suggest that the concomitant increases in both excitatory and inhibitory connections do not necessarily lead to increased pairwise activity correlations. Since our analysis cannot identify which of the inputs are active together, it is likely that increased balanced connectivity can lead to an increase in noncoincident activity sources to individual neurons, which can act to decorrelate their activity. However, a limitation of our comparison is that our in vivo data are restricted to neurons within a few hundred microns of each other. In contrast, our LSPS method does not allow us to probe excitatory connections at such close range due to the direct activation of GluRs on the patched cell, but does allow us to measure inputs from up to 1 mm away. Thus, we cannot exclude the possibility that very local (<100 μm) excitatory connections decrease with age and that cells at very large distances might show increased correlations. Nevertheless, our data show that pairwise NCs in L2/3 and L4 are highest at P9–11, which is consistent with neighboring cells being highly connected either via chemical or electrical synapses (Peinado et al. 1993; Levy and Reyes 2012; Li et al. 2012; Ohtsuki et al. 2012; Ko et al. 2013).

Overall, we describe distinct changes in laminar connectivity and organization of A1 during development and identify transient hyperconnectivity between subgranular layers (L5/6) and supragranular layers (L2/3) during the critical period. Specifically, our results suggest that subgranular input to L4 and L2/3 might play an important role in plasticity during the critical period.

## Supplementary Material

Supplementary material  is available at *Cerebral Cortex* online.

## Funding

## Notes

## References

Adelsberger H, Garaschuk O, Konnerth A. 2005. Cortical calcium waves in resting newborn mice. *Nat Neurosci*. 8:988–990.

Atencio CA, Schreiner CE. 2010. Columnar connectivity and laminar processing in cat primary auditory cortex. *PLoS One*. 5:e9521.

Atencio CA, Sharpee TO, Schreiner CE. 2009. Hierarchical computation in the canonical auditory cortical circuit. *Proc Natl Acad Sci U S A*. 106:21894–21899.

Averbeck BB, Latham PE, Pouget A. 2006. Neural correlations, population coding and computation. *Nat Rev Neurosci*. 7:358–366.

Babola TA, Li S, Gribizis A, Lee BJ, Issa JB, Wang HC, Crair MC, Bergles DE. 2018. Homeostatic control of spontaneous activity in the developing auditory system. *Neuron*. 99:511–524 e515.

Bandyopadhyay S, Shamma SA, Kanold PO. 2010. Dichotomy of functional organization in the mouse auditory cortex. *Nat Neurosci*. 13:361–368.

Banks MI, Uhlrich DJ, Smith PH, Krause BM, Manning KA. 2011. Descending projections from extrastriate visual cortex modulate responses of cells in primary auditory cortex. *Cereb Cortex*. 21:2620–2638.

Barkat TR, Polley DB, Hensch TK. 2011. A critical period for auditory thalamocortical connectivity. *Nat Neurosci*. 14:1189–1194.

Bortone DS, Olsen SR, Scanziani M. 2014. Translaminar inhibitory cells recruited by layer 6 corticothalamic neurons suppress visual cortex. *Neuron*. 82:474–485.

Caras ML, Sanes DH. 2015. Sustained perceptual deficits from transient sensory deprivation. *J Neurosci*. 35:10831–10842.

Carrasco MM, Trujillo M, Razak K. 2013. Development of response selectivity in the mouse auditory cortex. *Hear Res*. 296:107–120.

Chambers AR, Resnik J, Yuan Y, Whitton JP, Edge AS, Liberman MC, Polley DB. 2016. Central gain restores auditory processing following near-complete cochlear denervation. *Neuron*. 89:867–879.

Chang EF, Merzenich MM. 2003. Environmental noise retards auditory cortical development. *Science*. 300:498–502.

Chen Q, Cichon J, Wang W, Qiu L, Lee SJ, Campbell NR, Destefino N, Goard MJ, Fu Z, Yasuda R *et al*. 2012. Imaging neural activity using Thy1-GCaMP transgenic mice. *Neuron*. 76:297–308.

Chen X, Leischner U, Rochefort NL, Nelken I, Konnerth A. 2011. Functional mapping of single spines in cortical neurons in vivo. *Nature*. 475:501–505.

Constantinople CM, Bruno RM. 2013. Deep cortical layers are activated directly by thalamus. *Science*. 340:1591–1594.

Crocker-Buque A, Brown SM, Kind PC, Isaac JT, Daw MI. 2015. Experience-dependent, layer-specific development of divergent thalamocortical connectivity. *Cereb Cortex*. 25:2255–2266.

Cruikshank SJ, Rose HJ, Metherate R. 2002. Auditory thalamocortical synaptic transmission in vitro. *J Neurophysiol*. 87:361–384.

Dana H, Chen TW, Hu A, Shields BC, Guo C, Looger LL, Kim DS, Svoboda K. 2014. Thy1-GCaMP6 transgenic mice for neuronal population imaging in vivo. *PLoS One*. 9:e108697.

De La Rocha J, Doiron B, Shea-Brown E, Josić K, Reyes A. 2007. Correlation between neural spike trains increases with firing rate. *Nature*. 448:802.

de Venecia RK, McMullen NT. 1994. Single thalamocortical axons diverge to multiple patches in neonatal auditory cortex. *Dev Brain Res*. 81:135–142.

de Villers-Sidani E, Chang EF, Bao S, Merzenich MM. 2007. Critical period window for spectral tuning defined in the primary auditory cortex (A1) in the rat. *J Neurosci*. 27:180–189.

Deng R, Kao JPY, Kanold PO. 2017. Distinct translaminar glutamatergic circuits to GABAergic interneurons in the neonatal auditory cortex. *Cell Rep*. 19:1141–1150.

Dorr A, Sled JG, Kabani N. 2007. Three-dimensional cerebral vasculature of the CBA mouse brain: a magnetic resonance imaging and micro computed tomography study. *NeuroImage*. 35:1409–1423.

Feldman DE. 2009. Synaptic mechanisms for plasticity in neocortex. *Annu Rev Neurosci*. 32:33–55.

Feller MB, Wellis DP, Stellwagen D, Werblin FS, Shatz CJ. 1996. Requirement for cholinergic synaptic transmission in the propagation of spontaneous retinal waves. *Science*. 272:1182–1187.

Francis NA, Winkowski DE, Sheikhattar A, Armengol K, Babadi B, Kanold PO. 2018. Small networks encode decision-making in primary auditory cortex. *Neuron*. 97:885.e886–897.e886.

Games KD, Winer JA. 1988. Layer V in rat auditory cortex: projections to the inferior colliculus and contralateral cortex. *Hear Res*. 34:1–25.

Garaschuk O, Linn J, Eilers J, Konnerth A. 2000. Large-scale oscillatory calcium waves in the immature cortex. *Nat Neurosci*. 3:452–459.

Geal-Dor M, Freeman S, Li G, Sohmer H. 1993. Development of hearing in neonatal rats: air and bone conducted ABR thresholds. *Hear Res*. 69:236–242.

Goncalves JT, Anstey JE, Golshani P, Portera-Cailliau C. 2013. Circuit level defects in the developing neocortex of fragile X mice. *Nat Neurosci*. 16:903–909.

Guo W, Chambers AR, Darrow KN, Hancock KE, Shinn-Cunningham BG, Polley DB. 2012. Robustness of cortical topography across fields, laminae, anesthetic states, and neurophysiological signal types. *J Neurosci*. 32:9159–9172.

Guo W, Clause AR, Barth-Maron A, Polley DB. 2017. A Corticothalamic circuit for dynamic switching between feature detection and discrimination. *Neuron*. 95:180.e185–194.e185.

Hackett TA, Barkat TR, O'Brien BM, Hensch TK, Polley DB. 2011. Linking topography to tonotopy in the mouse auditory thalamocortical circuit. *J Neurosci*. 31:2983–2995.

Hanganu IL, Ben-Ari Y, Khazipov R. 2006. Retinal waves trigger spindle bursts in the neonatal rat visual cortex. *J Neurosci*. 26:6728–6736.

Hensch TK. 2004. Critical period regulation. *Annu Rev Neurosci*. 27:549–579.

Hoerder-Suabedissen A, Hayashi S, Upton L, Nolan Z, Casas-Torremocha D, Grant E, Viswanathan S, Kanold PO, Clasca F, Kim Y *et al*. 2018. Subset of cortical layer 6b neurons selectively innervates higher order thalamic nuclei in mice. *Cereb Cortex*. 28:1882–1897.

Hromadka T, Deweese MR, Zador AM. 2008. Sparse representation of sounds in the unanesthetized auditory cortex. *PLoS Biol*. 6:e16.

Insanally MN, Kover H, Kim H, Bao S. 2009. Feature-dependent sensitive periods in the development of complex sound representation. *J Neurosci*. 29:5456–5462.

Intskirveli I, Joshi A, Vizcarra-Chacón BJ, Metherate R. 2016. Spectral breadth and laminar distribution of thalamocortical inputs to A1. *J Neurophysiol*. 115:2083–2094.

Ji X-y, Zingg B, Mesik L, Xiao Z, Zhang LI, Tao HW. 2015. Thalamocortical innervation pattern in mouse auditory and visual cortex: laminar and cell-type specificity. *Cereb Cortex*. 26:2612–2625.

Kalmbach AS, Waters J. 2012. Brain surface temperature under a craniotomy. *J Neurophysiol*. 108:3138–3146.

Kanold PO, Nelken I, Polley DB. 2014. Local versus global scales of organization in auditory cortex. *Trends Neurosci*. 37:502–510.

Kanold PO, Shatz CJ. 2006. Subplate neurons regulate maturation of cortical inhibition and outcome of ocular dominance plasticity. *Neuron*. 51:627–638.

Kanold PO. 2009. Subplate neurons: crucial regulators of cortical development and plasticity. *Front Neuroanat*. 3:16. doi:10.3389/neuro.05.016.2009. eCollection 2009.

Kanold PO, Luhmann HJ. 2010. The subplate and early cortical circuits. *Annu Rev Neurosci*. 33:23–48. doi:10.1146/annurev-neuro-060909-153244.

Kerlin AM, Andermann ML, Berezovskii VK, Reid RC. 2010. Broadly tuned response properties of diverse inhibitory neuron subtypes in mouse visual cortex. *Neuron*. 67:858–871.

Kim J, Matney CJ, Blankenship A, Hestrin S, Brown SP. 2014. Layer 6 corticothalamic neurons activate a cortical output layer, layer 5a. *J Neurosci*. 34:9656–9664.

Ko H, Cossell L, Baragli C, Antolik J, Clopath C, Hofer SB, Mrsic-Flogel TD. 2013. The emergence of functional microcircuits in visual cortex. *Nature*. 496:96–100.

Levy RB, Reyes AD. 2012. Spatial profile of excitatory and inhibitory synaptic connectivity in mouse primary auditory cortex. *J Neurosci*. 32:5609–5619.

Li Y, Lu H, Cheng PL, Ge S, Xu H, Shi SH, Dan Y. 2012. Clonally related visual cortical neurons show similar stimulus feature selectivity. *Nature*. 486:118–121.

Liang F, Li H, Chou XL, Zhou M, Zhang NK, Xiao Z, Zhang KK, Tao HW, Zhang LI. 2018. Sparse representation in awake auditory cortex: cell-type dependence, synaptic mechanisms, developmental emergence, and modulation. *Cereb Cortex*. 2018 Oct 11. doi:10.1093/cercor/bhy260. [Epub ahead of print].

Liu J, Whiteway MR, Sheikhattar A, Butts DA, Babadi B, Kanold PO. 2019. Parallel processing of sound dynamics across mouse auditory cortex via spatially patterned thalamic inputs and distinct areal Intracortical circuits. *Cell Rep*. 27:872–885 e877.

Maor I, Shalev A, Mizrahi A. 2016. Distinct spatiotemporal response properties of excitatory versus inhibitory neurons in the mouse auditory cortex. *Cereb Cortex*. 26:4242–4252.

Marx M, Qi G, Hanganu-Opatz IL, Kilb W, Luhmann HJ, Feldmeyer D. 2017. Neocortical layer 6B as a remnant of the subplate—a morphological comparison. *Cereb Cortex*. 27:1011–1026.

McMullen NT, Goldberger B, Glaser EM. 1988. Postnatal development of lamina III/IV nonpyramidal neurons in rabbit auditory cortex: quantitative and spatial analyses of Golgi-impregnated material. *J Comp Neurol*. 278:139–155.

Mease RA, Metz M, Groh A. 2016. Cortical sensory responses are enhanced by the higher-order thalamus. *Cell Rep*. 14:208–215.

Meng X, Kao JP, Kanold PO. 2014. Differential signaling to subplate neurons by spatially specific silent synapses in developing auditory cortex. *J Neurosci*. 34:8855–8864.

Meng X, Kao JP, Lee HK, Kanold PO. 2015. Visual deprivation causes refinement of intracortical circuits in the auditory cortex. *Cell Rep*. 12:955–964.

Meng X, Kao JP, Lee HK, Kanold PO. 2017a. Intracortical circuits in thalamorecipient layers of auditory cortex refine after visual deprivation. *eNeuro, 3 April 2017*. 4(2). ENEURO.0092-17.2017; doi:https://doi.org/10.1523/ENEURO.0092-17.2017.

Meng X, Winkowski DE, Kao JPY, Kanold PO. 2017b. Sublaminar subdivision of mouse auditory cortex layer 2/3 based on functional Translaminar connections. *J Neurosci*. 37:10200–10214.

Morrill RJ, Hasenstaub AR. 2018. Visual information present in Infragranular layers of mouse auditory cortex. *J Neurosci*. 38:2854–2862.

Mowery TM, Kotak VC, Sanes DH. 2015. Transient hearing loss within a critical period causes persistent changes to cellular properties in adult auditory cortex. *Cereb Cortex*. 25:2083–2094.

Muralidharan S, Dirda ND, Katz EJ, Tang CM, Bandyopadhyay S, Kanold PO, Kao JP. 2016. Ncm, a photolabile group for preparation of caged molecules: synthesis and biological application. *PLoS One*. 11:e0163937.

Nelson A, Schneider DM, Takatoh J, Sakurai K, Wang F, Mooney R. 2013. A circuit for motor cortical modulation of auditory cortical activity. *J Neurosci*. 33:14342–14353.

Ohtsuki G, Nishiyama M, Yoshida T, Murakami T, Histed M, Lois C, Ohki K. 2012. Similarity of visual selectivity among clonally related neurons in visual cortex. *Neuron*. 75:65–72.

Olsen SR, Bortone DS, Adesnik H, Scanziani M. 2012. Gain control by layer six in cortical circuits of vision. *Nature*. 483: 47–52.

Oviedo HV, Bureau I, Svoboda K, Zador AM. 2010. The functional asymmetry of auditory cortex is reflected in the organization of local cortical circuits. *Nat Neurosci*. 13:1413–1420.

Peinado A, Yuste R, Katz LC. 1993. Extensive dye coupling between rat neocortical neurons during the period of circuit formation. *Neuron*. 10:103–114.

Peron SP, Freeman J, Iyer V, Guo C, Svoboda K. 2015. A cellular resolution map of barrel cortex activity during tactile behavior. *Neuron*. 86:783–799.

Petrof I, Viaene AN, Sherman SM. 2012. Two populations of corticothalamic and interareal corticocortical cells in the subgranular layers of the mouse primary sensory cortices. *J Comp Neurol*. 520:1678–1686.

Prieto JJ, Winer JA. 1999. Layer VI in cat primary auditory cortex: Golgi study and sublaminar origins of projection neurons. *J Comp Neurol*. 404:332–358.

Ratzlaff EH, Grinvald A. 1991. A tandem-lens epifluorescence macroscope: hundred-fold brightness advantage for widefield imaging. *J Neurosci Methods*. 36:127–137.

Rothschild G, Cohen L, Mizrahi A, Nelken I. 2013. Elevated correlations in neuronal ensembles of mouse auditory cortex following parturition. *J Neurosci*. 33:12851–12861.

Rothschild G, Nelken I, Mizrahi A. 2010. Functional organization and population dynamics in the mouse primary auditory cortex. *Nat Neurosci*. 13:353–360.

Schachtele SJ, Losh J, Dailey ME, Green SH. 2011. Spine formation and maturation in the developing rat auditory cortex. *J Comp Neurol*. 519:3327–3345.

Schneider DM, Nelson A, Mooney R. 2014. A synaptic and circuit basis for corollary discharge in the auditory cortex. *Nature*. 513:189.

Schreiner CE, Polley DB. 2014. Auditory map plasticity: diversity in causes and consequences. *Curr Opin Neurobiol*. 24: 143–156.

Schreiner CE, Winer JA. 2007. Auditory cortex mapmaking: principles, projections, and plasticity. *Neuron*. 56:356–365.

Schroeder CE, Foxe JJ. 2002. The timing and laminar profile of converging inputs to multisensory areas of the macaque neocortex. *Brain Res Cogn Brain Res*. 14:187–198.

Sheikh A, Meng X, Liu J, Mikhailova A, Kao JPY, McQuillen PS, Kanold PO. 2019. Neonatal hypoxia-ischemia causes functional circuit changes in subplate neurons. *Cereb Cortex*. 29:765–776.

Shepherd GM, Pologruto TA, Svoboda K. 2003. Circuit analysis of experience-dependent plasticity in the developing rat barrel cortex. *Neuron*. 38:277–289.

Siegel F, Heimel JA, Peters J, Lohmann C. 2012. Peripheral and central inputs shape network dynamics in the developing visual cortex in vivo. *Curr Biol*. 22:253–258.

Slater BJ, Yudintsev G, Lee CM, Llano DA. 2019. Thalamocortical and intracortical inputs differentiate layer-specific mouse auditory corticocollicular neurons. *J Neurosci*. 39:256–270.

Stiebler I, Neulist R, Fichtel I, Ehret G. 1997. The auditory cortex of the house mouse: left-right differences, tonotopic organization and quantitative analysis of frequency representation. *J Comp Physiol A*. 181:559–571.

Sun YJ, Wu GK, Liu BH, Li P, Zhou M, Xiao Z, Tao HW, Zhang LI. 2010. Fine-tuning of pre-balanced excitation and inhibition during auditory cortical development. *Nature*. 465:927–931.

Suter BA, O'Connor T, Iyer V, Petreanu LT, Hooks BM, Kiritani T, Svoboda K, Shepherd GM. 2010. Ephus: multipurpose data acquisition software for neuroscience experiments. *Front Neural Circuits*. 4:100.

Tischbirek CH, Noda T, Tohmi M, Birkner A, Nelken I, Konnerth A. 2019. In vivo functional mapping of a cortical column at single-neuron resolution. *Cell Rep*. 27:1319.e5–1326.e5.

Trachtenberg JT, Stryker MP. 2001. Rapid anatomical plasticity of horizontal connections in the developing visual cortex. *J Neurosci*. 21:3476–3482.

Trachtenberg JT, Trepel C, Stryker MP. 2000. Rapid extragranular plasticity in the absence of thalamocortical plasticity in the developing primary visual cortex. *Science*. 287:2029–2032.

Tritsch NX, Rodriguez-Contreras A, Crins TT, Wang HC, Borst JG, Bergles DE. 2010. Calcium action potentials in hair cells pattern auditory neuron activity before hearing onset. *Nat Neurosci*. 13:1050–1052.

Tritsch NX, Yi E, Gale JE, Glowatzki E, Bergles DE. 2007. The origin of spontaneous activity in the developing auditory system. *Nature*. 450:50–55.

Vélez-Fort M, Margrie TW. 2012. Cortical circuits: layer 6 is a gain changer. *Curr Biol*. 22:R411–R413.

Viswanathan S, Bandyopadhyay S, Kao JP, Kanold PO. 2012. Changing microcircuits in the subplate of the developing cortex. *J Neurosci*. 32:1589–1601.

Viswanathan S, Sheikh A, Looger LL, Kanold PO. 2017. Molecularly defined subplate neurons project both to thalamocortical recipient layers and thalamus. *Cereb Cortex*. 27: 4759–4768.

Wang HC, Bergles DE. 2015. Spontaneous activity in the developing auditory system. *Cell Tissue Res*. 361:65–75.

Wess JM, Isaiah A, Watkins PV, Kanold PO. 2017. Subplate neurons are the first cortical neurons to respond to sensory stimuli. *Proc Natl Acad Sci U S A*. 114:12602–12607.

Williamson RS, Polley DB. 2019. Parallel pathways for sound processing and functional connectivity among layer 5 and 6 auditory corticofugal neurons. *elife*. 8:e42974.

Willott JF, Shnerson A. 1978. Rapid development of tuning characteristics of inferior colliculus neurons of mouse pups. *Brain Res*. 148:230–233.

Winer JA, Prieto JJ. 2001. Layer V in cat primary auditory cortex (AI): cellular architecture and identification of projection neurons. *J Comp Neurol*. 434:379–412.

Winkowski DE, Kanold PO. 2013. Laminar transformation of frequency organization in auditory cortex. *J Neurosci*. 33:1498–1508.

Winkowski DE, Nagode DA, Donaldson KJ, Yin P, Shamma SA, Fritz JB, Kanold PO. 2018. Orbitofrontal cortex neurons respond to sound and activate primary auditory cortex neurons. *Cereb Cortex*. 28:868–879.

Zhang LI, Bao S, Merzenich MM. 2001. Persistent and specific influences of early acoustic environments on primary auditory cortex. *Nat Neurosci*. 4:1123–1130.

Zhao C, Kao JP, Kanold PO. 2009. Functional excitatory microcircuits in neonatal cortex connect thalamus and layer 4. *J Neurosci*. 29:15479–15488.